Research Square

Preprints are preliminary reports that have not undergone peer review.
They should not be considered conclusive, used to inform clinical practice,
or referenced by the media as validated information.

Dynamic Response Characteristics of Metro Curved Tracks under Asymmetric Wheel Flat Excitations

Zijie Xu
Jiangsu Normal University
Xiang Li
lixiangjsnu@163.com
Jiangsu Normal University
Xinlei He
Beijing Jiaotong University
Zunsong Ren
Beijing Jiaotong University
Sisi Li
Jiangsu Normal University
Hui Fan
Jiangsu Normal University

Research Article

Keywords: Multibody dynamics, Asymmetric wheel flat, Metro curve, Rigid–flexible coupling, Vibration characteristics

Posted Date: April 28th, 2026

DOI: https://doi.org/10.21203/rs.3.rs-9406506/v1

License: This work is licensed under a Creative Commons Attribution 4.0 International License.
Read Full License

Additional Declarations: No competing interests reported.

Dynamic Response Characteristics of Metro Curved Tracks under Asymmetric Wheel Flat Excitations

Zijie Xu[1]·Xiang Li[1*]·Xinlei He[2]·Zunsong Ren[2]·Sisi Li[1]·Hui Fan[1]

Abstract

Wheel flats are common defects in railway systems and are known to generate high-frequency impact forces and vibrations during vehicle operation. In the study, a vehicle–track coupled dynamic model is developed to investigate the wheel–rail impact induced by the coupled effect of dual wheel flats under a special operating condition, namely curved track sections. The study focuses on evaluating the influence of such dual-flat coupling on wheel–rail interaction and on the dynamic response of the track system. The key findings are as follows: (1) The length and phase difference of outer-wheel flats strongly affect the wheel–rail vertical force and the corresponding the power spectral density(PSD) amplitudes. When the outer-flat length reaches 50 mm with a phase difference of 25°–30°, the outer-wheel vertical force peaks at 507.68 kN, representing the maximum dynamic amplification. (2) The inner rail consistently exhibits higher responses than the outer rail. Dominant frequency peaks occur at 18.89 Hz (fifth vertical bending mode of the rail) and 13.33 Hz (fourth bending mode of the track slab), indicating that the system response is governed by the structural natural frequencies. (3) Phase-offset dual flats may induce localized superposition or cancellation effects and excite higher-order structural modes, leading to resonance at 36 Hz and 60 Hz. These results indicate that wheel flats mainly influence the dynamic response by modulating vibration amplitude and energy distribution, whereas peak frequencies are governed by the structural natural modes. The identified mechanisms provide insights for track-condition monitoring, defect diagnosis, and fatigue-life prediction.

Keywords Multibody dynamics·Asymmetric wheel flat·Metro curve·Rigid–flexible coupling·Vibration characteristics.

Zijie Xu
Xuzijie1107@outlook.com
Xiang Li
lixiangjsnu@163.com
Xinlei He
25121113@bjtu.edu.cn
Zunsong Ren
zsren@bjtu.edu.cn
Sisi Li
1312208937@qq.com
Hui Fan
xzfanhui@163.com

[1] School of Mechatronic Engineering, Jiangsu Normal University, No. 101, Shanghai Road, Tongshan New District, Xuzhou City, Jiangsu Province 221116, China

[2] School of Mechanical, Electronic and Control Engineering, Beijing Jiaotong University, No. 3 Shangyuan Village, Haidian District, Beijing 100044, China

*Corresponding author

1 Introduction

With the rapid development of high-speed rail and urban rail transit, train operating speeds have continuously increased, making the dynamic behavior of the wheel–rail system a critical factor affecting operational safety and reliability. In practice, wheel defects—including wheel flats and polygonization—as well as rail corrugation, are the primary sources of severe vibration and noise in vehicle–track systems. These defects not only accelerate the deterioration of both rolling stock and track structures but also significantly compromise passenger comfort and operational safety. Consequently, extensive research has been conducted worldwide on the formation mechanisms, dynamic characteristics, detection and diagnostic techniques, and mitigation strategies for these phenomena, yielding substantial progress.

In wheel-flat research, Zhai et al.[1] developed a theoretical model and simulation software (VICT) based on vehicle–track coupled dynamics, showing that wheel flats most adversely affect track responses at speeds of 140–160 km/h, particularly at turnouts, rail joints, and bridge–embankment transitions. Zhu et al.[2] employed an adaptive contact model with a three-dimensional vehicle–track system to reveal that impacts from subsequent flats depend strongly on the geometry, relative positions, and speeds of preceding flats, indicating that wheel-flat length alone is insufficient for discard criteria. Ren[3] demonstrated that the width, length, and width-to-length ratio of flats significantly influence impact severity, and proposed safe operational domains considering speed and defect size. Li et al.[4] combined a 56-degree-of-freedom vehicle model with an adaptive multi-scale morphological filtering (AMMF) algorithm, enabling real-time extraction of axle-box vibration features for wheel-flat diagnosis. Zhou et al.[5] developed a multi-sensor fusion method with angle-domain synchronous averaging (ADSA) to accurately detect and locate wheel-flat impacts under complex conditions. Magalhães et al.[6] proposed an unsupervised approach integrating virtual wayside monitoring with a sparse autoencoder network for identifying wheel flats and polygonal wheels across varying speeds and track irregularities. Fu et al.[7] systematically reviewed acoustic, image-based, stress-based, and signal-processing detection methods, highlighting future directions in equipment simplification, multi-sensor fusion, and machine-learning-based intelligent detection. Uzzal et al.[8] further examined the effects of multiple wheel flats on bogie vibration modes and proposed an intelligent detection scheme based on multi-defect response features.

In wheel-polygonization research, it has been observed that wheel flats can gradually evolve into polygonal wheels. Nielsen et al.[9] reviewed the causes, development mechanisms, and damage processes of long-wavelength polygonal wheels, systematically summarizing detection methods, predictive models, discard criteria, and measures to slow their progression. Jin et al.[10] investigated the resonant mechanisms of metro wheel polygonization through field measurements and model tests, finding that excitation occurs when operational frequencies approach the first bending natural frequency of wheelset, thereby dominating axle-box vibrations. They also noted that polygonal wear accelerates following heavy re-profiling. Ye et al.[11] developed a coupled dynamic model of a direct-drive locomotive, showing that wheel polygonization significantly amplifies vibrations of critical electric drive components and leaves characteristic frequencies in electrical signals, highlighting its potential for condition monitoring. Xu et al.[12] demonstrated that, for high-speed trains at 350–400 km/h, 20th-order polygonal wheels can excite high-frequency vibrations (60–84 Hz), increasing wheel–rail force fluctuations, rail-climbing risk, and resonance with flexible carbody modes. They further proposed measures to limit vibration amplitudes below 0.05 mm. Ye et al.[13], using track modal tests and dynamic simulations, revealed that 18th–23rd-order polygonal wheels arise from the near coincidence of the third-order bending mode of track and wheel polygonization frequency. Wang et al.[14] experimentally showed that flexible resonance induced by wheel irregularities is the primary cause of abnormal vibrations, and that heavy re-profiling can improve ride comfort by 35–40% and reduce the vibration of axle-box by approximately 40%.

During train operations, wheel irregularities and rail corrugation produce superimposed excitations that accelerate contact wear and compromise safety and ride comfort. Hu et al.[15] developed a coupled vehicle–switch model, revealing that turnout corrugation is concentrated at wavelengths of 80–110 mm and depths of 0.25–0.30 mm, dominated by rail bending vibrations at 76–173 Hz, and it shortens the wheel-loaded transition zone, significantly affecting dynamic responses. Cui et al.[16] through field monitoring and dynamic analysis, found that hollow wear induces double balance points and “pseudo-flange vibrations,” while side wear generates negative effective conicity, causing wheelsets to deviate from the track centerline

*Corresponding author

and affecting stability and comfort. They also proposed re-profiling thresholds and identified vibration energy accumulation, uneven local friction work, and phase shifts as key drivers of rail corrugation evolution. Luo et al.[17] combining experiments and simulations, developed a rigid–flexible coupled bogie model, showing that bogie frames possess natural frequencies independent of track geometry, and that vibration-reducing tracks such as floating slabs and trapezoidal sleepers can reduce structural damage by at least 8.9%, with curved sections experiencing greater damage than straight sections. Wang et al.[18] proposed an unsupervised detection method using carbody vertical acceleration signals and synchronous wavelet packet transform, achieving 98.6% accuracy and over 95% wavelength classification precision without labeled data. Wang et al.[19, 20] through field and finite element studies, revealed excitation modes of rail corrugation and suggested adjusting fastener and spring stiffness to modify track natural frequencies, their vehicle–track system model further showed that deepened corrugation amplifies stick–slip vibrations from wheel flats, whereas increased flat depth may reduce corrugation-induced stick–slip effects. Wu et al.[21] established a 3D finite element model to examine friction-induced vibrations and short-wavelength corrugation, finding that wheel-spoke geometry, flange thickness, and axial dimensions significantly influence corrugation occurrence, and proposed structural optimization strategies.

To improve passenger safety and ride comfort, structural vibration suppression and isolation measures have been widely applied. Zhu et al.[22] proposed a “harden-then-soften” (HFTS) nonlinear floating-slab isolator, effectively balancing displacement restraint with low-frequency vibration isolation and significantly reducing tunnel acceleration responses. Luo et al.[23] developed a finite element model incorporating wheel–brake block contact and heat conduction, introducing a non-uniform heat flux reconstruction method; their results showed that local temperature rises due to wheel flats can exceed the critical austenite transformation threshold, posing potential thermal damage risks. Li[24], through rigid–flexible coupled vehicle–track dynamic analysis of vibration-reducing track structures, demonstrated that track vibration characteristics and wheel–rail contact stresses are key factors in the formation of rail corrugation in metro systems.

In summary, despite significant advances in wheel-defect modeling, rail corrugation mechanisms, dynamic response analysis, and intelligent detection methods, several limitations persist. Most studies remain restricted to straight tracks and idealized conditions, providing limited insight into the complex wheel–rail dynamics on curves. Experiments and simulations often rely on theoretical design speeds rather than measured operational speeds during curve negotiation, resulting in discrepancies with real-world conditions. Additionally, wheel wear is frequently idealized as symmetric, overlooking the asymmetric wear patterns commonly observed after prolonged train operation on curved sections. Finally, while prior research has focused largely on single wheel-flat excitations, systematic studies on the superimposed effects and interactions of dual or multiple wheel-flat combinations are still lacking.

Based on the aforementioned limitations, the innovations of this study are as follows:

(1) focusing on curved tracks to more closely represent actual operational conditions;

(2) incorporating measured train speeds during curve negotiation to enhance the realism and engineering applicability of the model;

(3) considering the actual asymmetric wheel-wear patterns in the modeling process, thereby providing a more accurate representation of wheel–rail contact and dynamic response characteristics;

(4) investigating dual wheel-flat excitations to reveal their compound effects on vehicle system vibrations and track responses. These improvements not only address the gaps in existing research but also offer new theoretical support and practical guidance for safe train operation and refined maintenance under curved-track conditions.

2 Vehicle Dynamics Modeling and Wheel-Flat Model

To investigate the influence of localized wheel flats on the dynamic response of the track system, a comprehensive vehicle–track coupled dynamic model was established, incorporating dual wheel-flat excitation conditions. By varying the spatial configuration and phase difference between the wheel flats, the coupled effects on wheel–rail contact forces and track structural vibrations were systematically analyzed. The results provide theoretical support for train operational safety assessment and track structure optimization.

*Corresponding author

2.1 Vehicle Dynamics Simulation Model

Based on vehicle dynamics theory, a vehicle–track coupled dynamic simulation model was established in SIMPACK to investigate the influence of wheel-flat excitation on track system vibrations. The basic parameters of model are shown in the Table 1[24].

Table 1 The basic parameters of model

Parameter name	Value	Unit
Bogie (frame) mass	2.63	t
Car body mass	28	t
Primary longitudinal stiffness	8.92	MN/m
Primary lateral stiffness	6.76	MN/m
Primary vertical stiffness	1.4	MN/m
Primary longitudinal damping	5	kN· s/m
Primary lateral damping	5	kN· s/m
Primary vertical damping	10	kN· s/m
Secondary longitudinal stiffness	0.32	MN/m
Secondary lateral stiffness	0.21	MN/m
Secondary vertical stiffness	0.48	MN/m
Secondary longitudinal damping	5	kN· s/m
Secondary lateral damping coefficient	50	kN· s/m
Secondary vertical damping	60	kN· s/m
Fastener vertical stiffness	40	kN/mm
Fastener longitudinal stiffness	8.79	kN/mm
Fastener lateral stiffness	8.79	kN/mm
Fastener vertical damping	9898	N· s/m
Steel spring vertical stiffness	6.6	kN/mm
Steel spring longitudinal stiffness	8	kN/mm
Steel spring lateral stiffness	8	kN/mm
Steel spring vertical damping	16700	N· s/m

As shown in Figure 1, the model mainly consists of a carbody, two bogies, four wheelsets(the wheel tread shape adopts LM), primary and secondary suspension systems, flexible rails(UIC60), rail fasteners, and flexible floating slabs, forming a rigid–flexible coupled vehicle–track dynamic system[24].

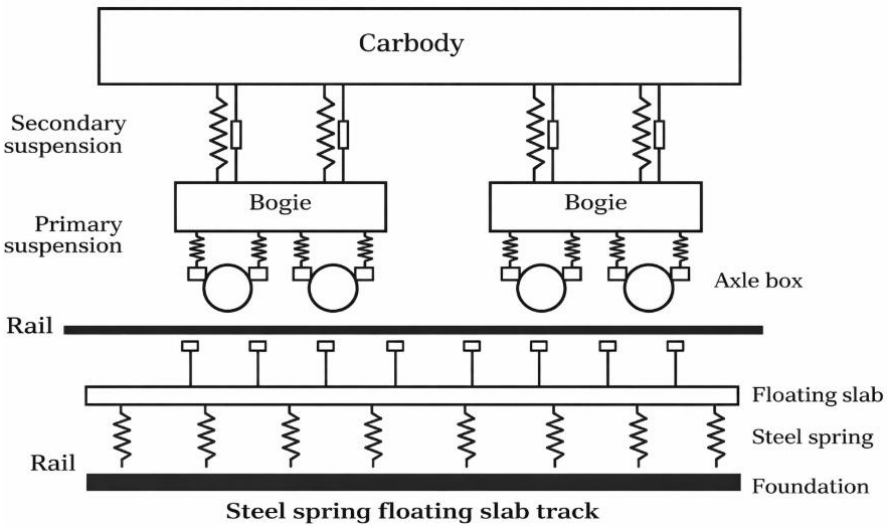


Fig. 1 Vehicle simulation model.

*Corresponding author

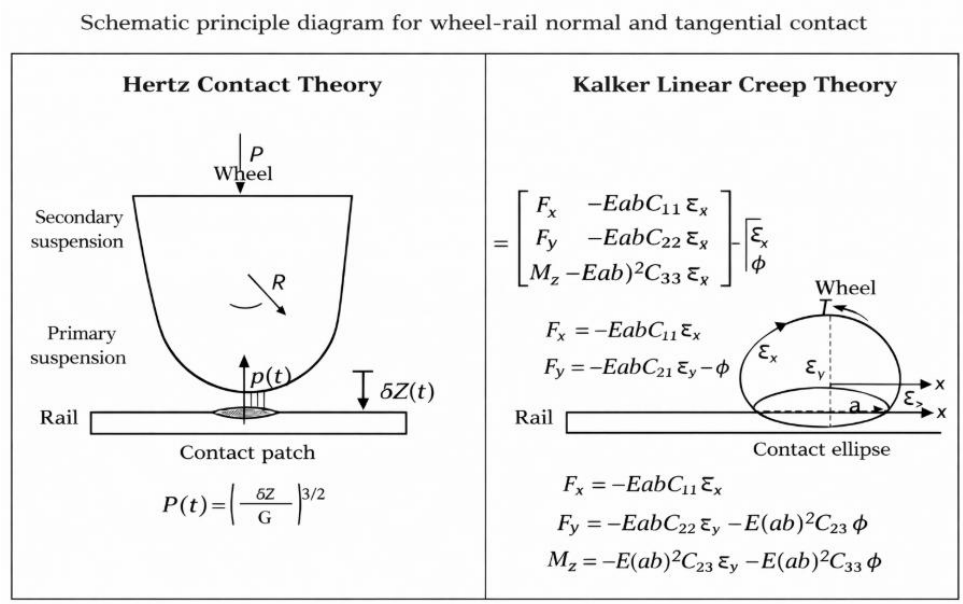


Fig. 2 Schematic diagram of wheel–rail contact based on Hertz contact theory and Kalker linear creep theory.

In the vehicle–track dynamic model, the wheel–rail contact force consists of normal and tangential components. In Figure 2, the vertical contact force is calculated by using the Hertz contact theory[28]:

$$P(t) = [\frac{1}{G}\delta Z(t)]^{3/2} \tag{1}$$

where G is the wheel-rail contact constant determined by the tread profile, and $\delta Z(t)$ denotes the vertical wheel-rail displacement. For a wheel with diameter R, the contact constant G for a worn tread can be written as:

$$G = 3.86R^{-0.115} \times 10^{-8} \tag{2}$$

the contact force is determined by the elastic compression between the wheel and rail and is proportional to the 3/2 power of the compression. The contact stiffness depends on the wheel–rail contact constant and the wheel radius.

The tangential contact forces are obtained based on Kalker's linear creep theory. Under the assumption of small creepage, the longitudinal creep force(T_x), lateral creep force(T_y), and spin creep moment(M_z) are linearly related to their corresponding creepages:

$$T_x = -f_{11}v_x \tag{3}$$

$$T_y = -f_{22}v_y - f_{23}v_z \tag{4}$$

$$M_z = -f_{32}v_y - f_{33}v_z \tag{5}$$

where v_x, v_y, and v_z represent the longitudinal, lateral, and spin creepages of the wheel–rail contact, respectively; f_{11} is the creep coefficient. The creep coefficients are determined by the geometric characteristics of the contact patch and the elastic properties of the materials. These coefficients are related to the semi-axes of the contact ellipse and the dimensionless Kalker coefficients. This formulation provides the necessary wheel–rail interaction forces for the vehicle dynamic analysis.

$$f_{11} = EabC_{11} \tag{6}$$

$$f_{12} = EabC_{22} \tag{7}$$

$$f_{23} = E(ab)^{\frac{3}{2}}C_{23} \tag{8}$$

$$f_{33} = E(ab)^2 \tag{9}$$

*Corresponding author

a and b denote the semi-major and semi-minor axes of the contact ellipse, respectively; and C_{ij} represents the dimensionless Kalker coefficient.

2.2 Calculation model considering slab and rail flexibility

The elastic characteristics of the track structure play a critical role in the wheel–rail coupled vibration response. To accurately capture the dynamic behavior of the track system under localized excitation, a flexible finite element modeling approach was adopted. The rails and track slabs were modeled as elastic components in ABAQUS, enabling a more realistic representation of the track system dynamics under wheel-flat excitation. The detailed modeling procedure is presented in Figure. 3.

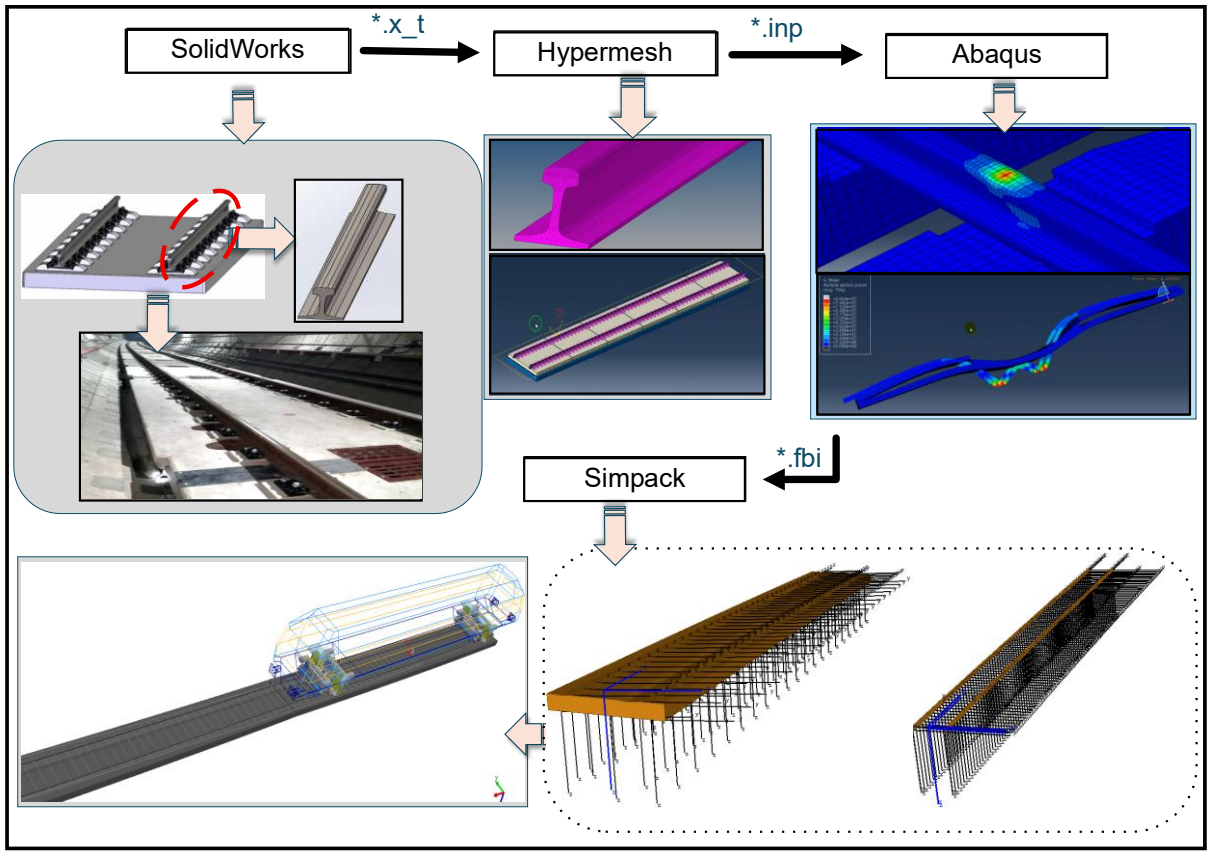


Fig. 3 Modeling flowchart.

To evaluate the dynamic response of the steel-spring floating slab track under wheel-flat excitation, its modal characteristics were analyzed. The system can be idealized as a mass–spring isolation system, where steel springs act as isolation elements between the floating slab and the trackbed, and the isolation performance is mainly governed by the natural frequencies of the lower-order modes. These modal properties determine both the deformation patterns of the track structure under wheel–rail forces and the vibration transmission characteristics of the elastic track system.

*Corresponding author

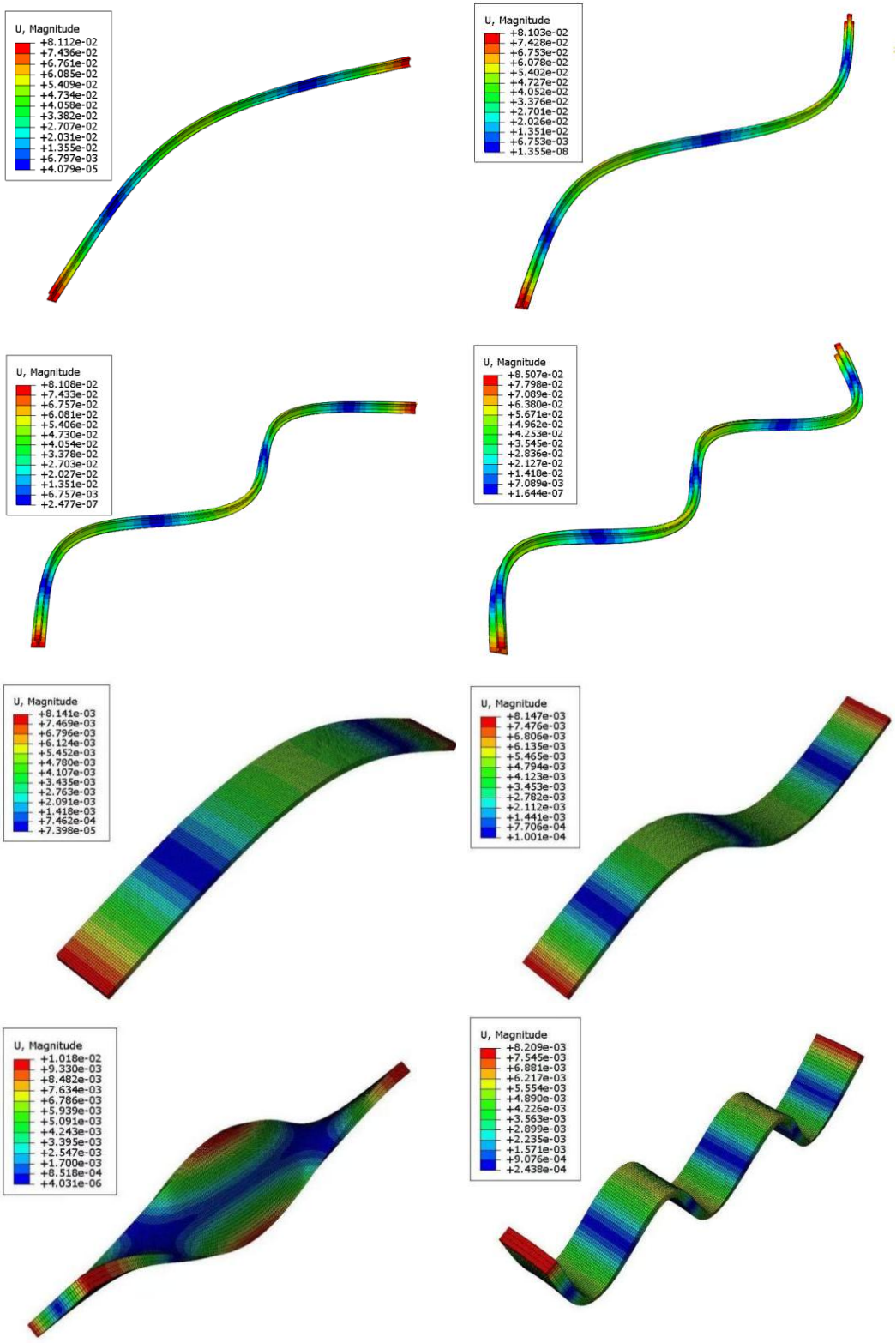
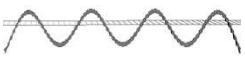
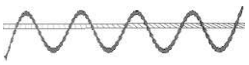
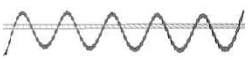


Fig. 4 Finite Element Mode Shape.

Therefore, modal analysis of the steel-spring floating slab track provides a basis for understanding the system response under multi-frequency excitation and supports flexible-body modeling. The corresponding modal shapes are shown in Table 2 and Figure 4.

*Corresponding author

Table 2 Modal characteristics of floading slab and rail.

Modal shape	Modal frequency		Modal shape	Modal frequency	
	Free mode	Constraint mode		Free mode	Constraint mode
	2.05Hz	1.42Hz		1.99Hz	1.42Hz
	5.65Hz	4.56Hz		5.17Hz	4.19Hz
	11.07Hz	9.44Hz		10.15Hz	8.74Hz
	18.30Hz	15.86Hz		16.74Hz	14.88Hz
	27.34Hz	20.82Hz		24.98Hz	22.61Hz
	38.20Hz	25.72Hz		34.80Hz	31.68Hz
	50.92Hz	35.41Hz		46.26Hz	39.23Hz
	65.54Hz	47.22Hz		59.23Hz	44.75Hz
	82.14Hz	60.70Hz		73.83Hz	56.28Hz
	100.81Hz	93.19Hz		89.22Hz	70.39Hz

2.3 Dynamic Model Validation

A rigid–flexible coupled dynamic model is established based on the SIMPACK. To improve computational efficiency, the model is appropriately simplified while preserving the essential dynamic characteristics. The fastening system is represented by marker points defined on the flexible bodies of the rail and the track slab, which are interconnected equivalent force elements. Similarly, the steel spring components are modeled as force elements, linking the marker points on the track slab to the ground to impose the boundary constraints. The schematic configuration of the model is illustrated in Figure. 5.

*Corresponding author

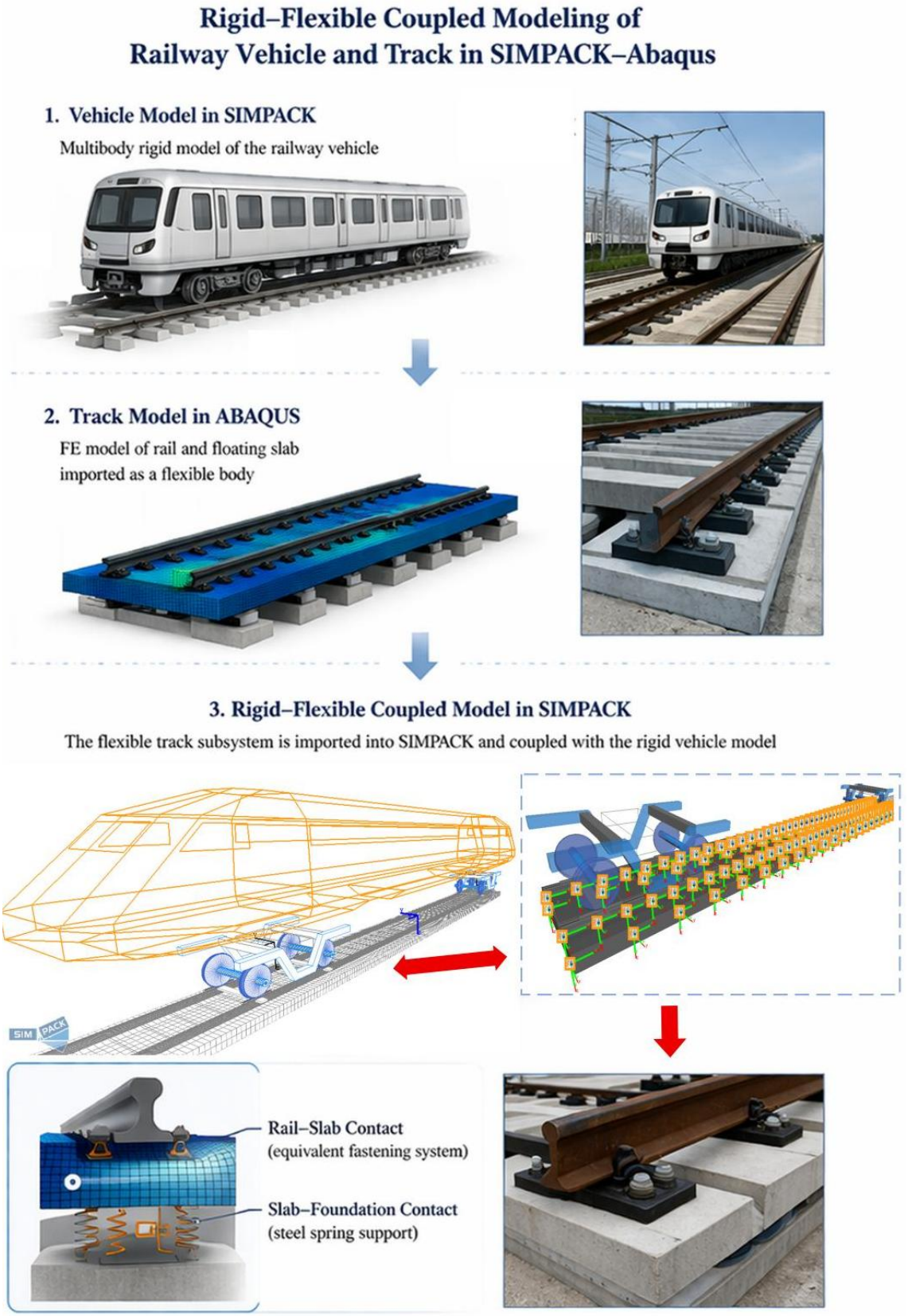


Fig. 5 Rigid–flexible coupled dynamic model.

As shown in Figure. 6, the time-domain simulation results were compared with the corresponding experimental data to verify the capability of the established vehicle dynamics model in characterizing the vibration responses of key components. Overall, the simulated results show good agreement with the

*Corresponding author

measured data and are able to reasonably reproduce the principal variation characteristics of the vehicle system vibration.

For the vertical accelerations of the left and right axle boxes[Figure. 6(a) and (b)], the simulation results generally capture the main fluctuation trends observed in the test data. In particular, the simulated response of the left axle box agrees well with the measured result over the entire time history, with only minor discrepancies appearing in several local intervals, especially near transient peaks. For the right axle box, although the overall fluctuation pattern remains basically consistent between simulation and experiment, the measured signal exhibits an evident baseline offset and does not oscillate strictly around zero. Considering the test conditions, this phenomenon is likely associated with sensor zero drift, installation conditions, and low-frequency noise interference.

For the frame vibration responses[Figure. 6(c) and (d)], the comparison reveals different levels of agreement in the vertical and lateral directions. In terms of vertical acceleration, the simulated curve presents a relatively regular evolution pattern, whereas the measured result contains stronger random fluctuations together with a certain degree of baseline drift, leading to noticeable differences in local amplitudes and detailed waveform characteristics. Nevertheless, the simulation still reproduces the overall development trend of the frame vertical vibration. In contrast, the simulated and measured results for frame lateral acceleration exhibit comparatively good consistency, particularly within the main oscillation interval, where the waveform evolution and attenuation characteristics are in close agreement. This indicates that the proposed model has a satisfactory capability in describing the lateral vibration behavior of the frame, although limited local deviations are still present.

In summary, the established model can effectively capture the dominant vibration responses of the vehicle system. The remaining discrepancies are mainly concentrated in local peak regions and are also influenced by random fluctuations and baseline drift in some measured signals. Since the currently available test data are still incomplete, the present study only provides a preliminary validation based on time-domain response trends and waveform consistency. A more comprehensive assessment will be conducted once more complete experimental data become available.

*Corresponding author

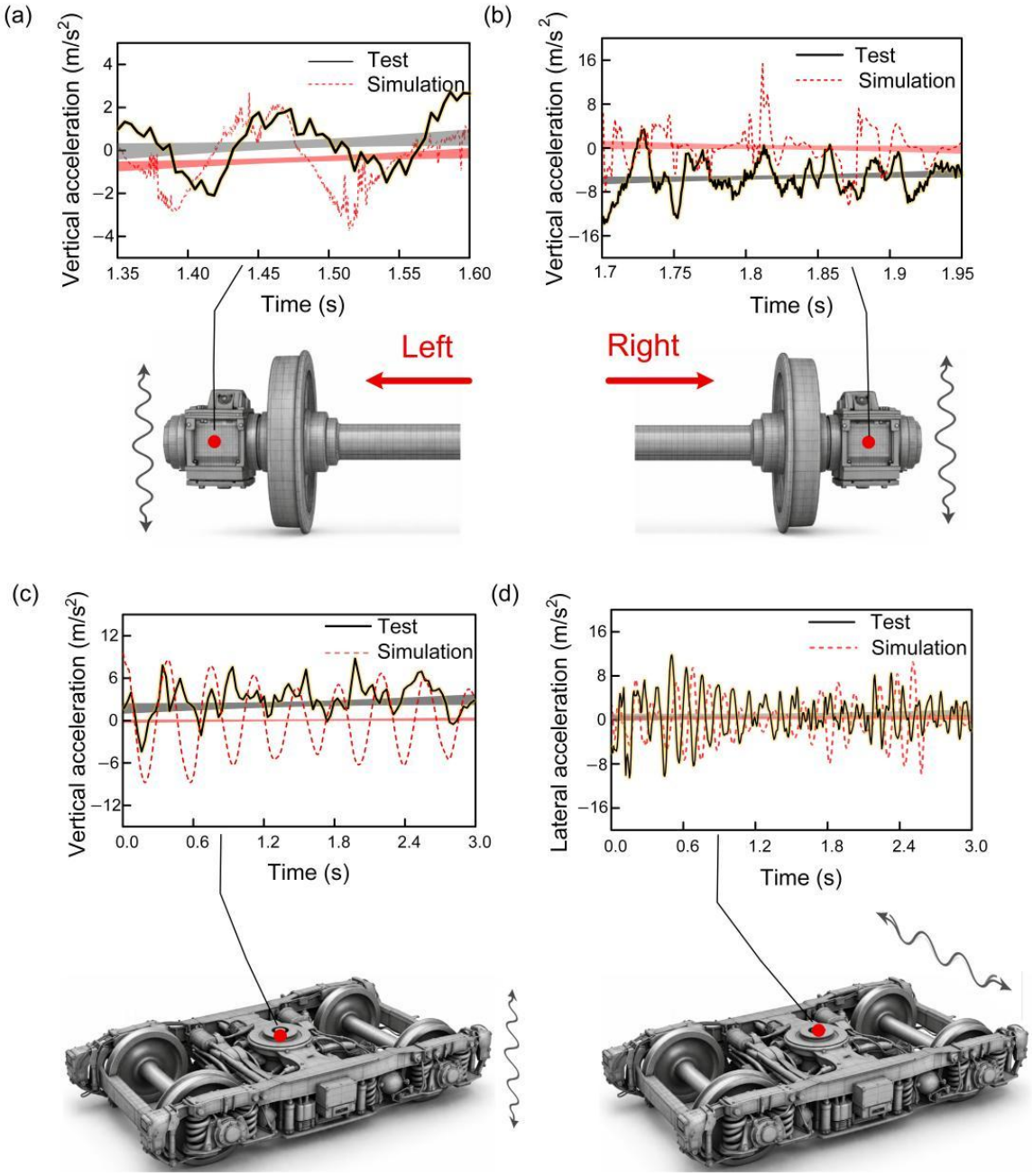


Fig. 6 Time-domain acceleration responses of axle box vertical and bogie frame lateral and vertical vibrations: (a) Axle box vertical acceleration(Left).(b) Axle box vertical acceleration(Right). (c) Bogie frame vertical acceleration. (d) Bogie frame lateral acceleration.

2.4 Modelling of Dual Wheel-Flat Excitations

Wheel flats are among the most common wheel tread defects in railway vehicles and pose a significant threat to operational safety. They are typically caused by wheel sliding or excessive slip during emergency braking, which produces severe friction and thermal damage at the wheel–rail contact interface, eventually forming localized flat spots, as illustrated in Figure. 7(a).

During train operation, these flats generate periodic impact loads that accelerate wheel–rail wear and induce abnormal vibration and noise.

*Corresponding author

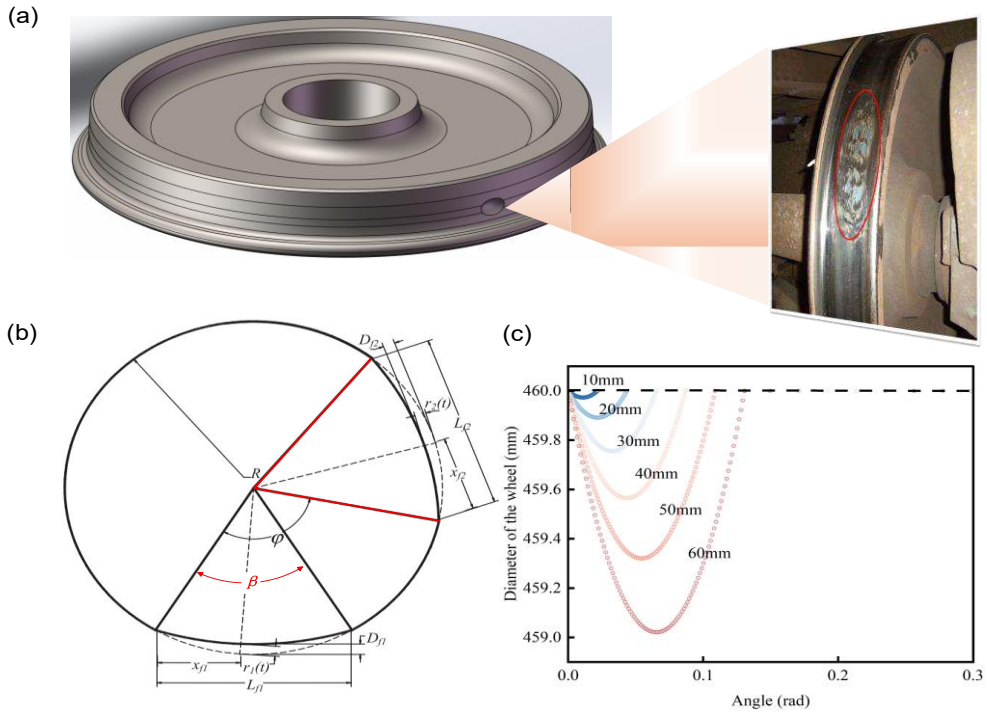


Fig. 7 Sketch of wheel flats: (a) sketch of wheel flat. (b) sketch of one wheel with two flats. (c) flat length.

Wheel flats can be classified as newly formed flats (new flats) and evolved flats (old flats). New flats typically have sharp edges that induce localized impacts and high-frequency vibrations during wheel–rail contact. With continued operation, repeated contact and wear gradually round these edges, forming old flats with smoother boundaries and reduced impact intensity.

This evolution modifies both the flat geometry and wheel–rail contact conditions, influencing the dynamic response of the track structure and potentially causing fatigue damage in key components such as rail fasteners and sleepers. To represent the excitation generated by evolved flats, an equivalent excitation model is adopted by modifying the wheelset diameter. The irregularity excitation is expressed as follows[8]:

$$d_i(t) = -\frac{1}{2}D_{fi}[1 - cos\,(\frac{2\pi x_{fi}}{L_{fi}})] \tag{10}$$

$$D_{fi} = \frac{L_{fi}^2}{16R} \quad i = 1,2 \tag{11}$$

where $d_i(t)$denotes the variation in wheel radius at the flat region with a length L_{fi} and depth D_{fi}. The parameter x_{fi} represents the arc length along the wheel surface, and R is the nominal wheel radius. By applying the measured flat-profile data along the wheel circumference using MATLAB, the radius variation in the flat region can be expressed as:

$$R_\beta = R - \frac{Ra^2}{8}[1 - cos\,(\frac{1}{a}\beta)] \tag{12}$$

$$a = \frac{L_{fi}}{2R} \tag{13}$$

Wheel flats may occur as a single defect (i = 1) or as two flats on the same wheel (i = 2). Here, β denotes the wheel rotation angle, whereas the phase angle represents the angular separation between the two flats on the same wheel, as illustrated in Fig. 7(b).

Based on the relative positions of flats on the two coaxial wheels, two representative configurations are considered: (1) in-phase and (2) out-of-phase. These configurations are used to examine the influence of dual wheel flats on the vibration behavior of the vehicle–track system. In addition, as shown in Fig. 7(c), typical flat lengths range from 10 to 60 mm, as commonly reported in the literature[8, 25, 27].

3 Dynamic Analysis under In-Phase Asymmetric Flats

*Corresponding author

During train operation on curved tracks, centrifugal forces and unequal wheel loads alter the wheel–rail contact state, strengthening inner-wheel contact and weakening outer-wheel contact. This uneven loading leads to non-uniform wear and may generate asymmetric wheel flats when sliding occurs. Because the inner and outer wheels experience different load and wear conditions, the resulting flats often differ in geometry and size.

Compared with symmetric flats, asymmetric flats can induce more complex dynamic responses in the track structure and increase risks to structural safety and service life. Therefore, the vibration behavior of the track system under asymmetric wheel-flat excitation is investigated. To ensure comparability, all simulations were performed under identical curved-track conditions using measured curve-negotiation speeds.

3.1 Wheel–Rail Dynamics Under In-Phase Asymmetric Flats

When a train negotiates a curved track, in-phase dual flats on coaxial wheels generate nearly simultaneous impact excitations during wheel–rail contact, as shown in Figure. 8(a). This coincidence promotes vibration superposition and amplifies the dynamic response of the vehicle–track system. The resulting impacts may also cause local stress concentrations in the track structure, potentially leading to fatigue damage and structural deterioration.

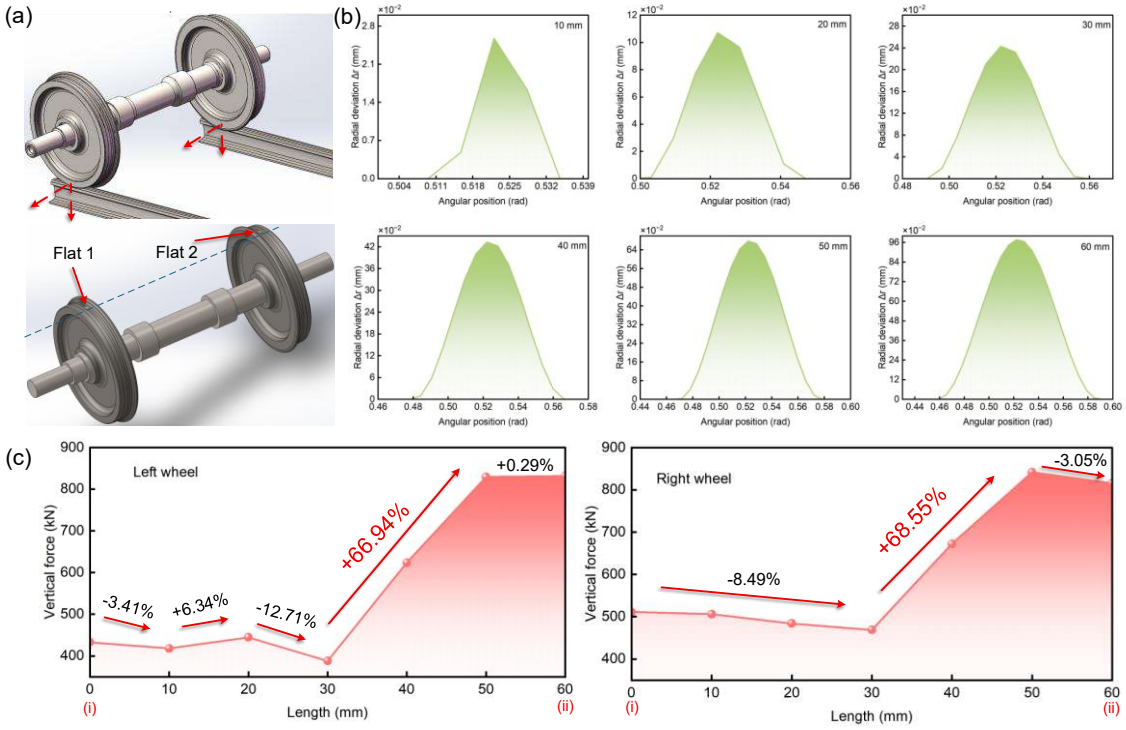


Fig. 8 Characteristic diagram of the flat and analysis of the maximum vertical force: (a) schematic diagram of wheel movement and flat position. (b) radial Deviation in Flat.. (c) maximum vertical force analysis of left and right wheels.

Considering the more severe wear of inner wheels on curved tracks, the inner-wheel flat length is fixed at 60 mm in this study, while the outer-wheel flat length is varied from 10 to 50 mm as the control parameter. As shown in Figure. 8(b), flat depth increases with flat length, making flat length the key geometric parameter describing the defect.

Two reference cases are defined for comparison: (i) no outer-wheel flat (0 mm) and (ii) a symmetric dual-flat condition with a 60 mm outer flat. These cases are used to evaluate the influence of asymmetric wheel-flat excitation on the dynamic response of the track system.

Unlike the monotonic increase observed for single flats, the outer-wheel vertical force under asymmetric dual-flat excitation shows a non-monotonic trend [Figure. 8(c)]. The force initially decreases by 3.41% as the flat length increases from 0 to 10 mm and reaches a minimum of 388.16 kN (−12.71%) at 30 mm. It then rises with increasing flat length, reaching 831.76 kN at 60 mm.

*Corresponding author

In contrast, the inner-wheel vertical force decreases by 8.49% as the flat length increases to 30 mm, then rises sharply by 68.55% at 50 mm before slightly decreasing by 3.05% at 60 mm. Both wheels reach their minimum vertical forces at 30 mm, indicating strong cancellation between the dual-flat excitations.

To further examine this effect, the inner-wheel flat is fixed at 60 mm while the outer flat is set to 30 mm and 50 mm. As shown in Fig. 9, flat length significantly alters the time history of wheel–rail forces. For a 30 mm outer flat, peak forces occur at 0.1–0.2 s with P_1 values of 495.83 kN (outer) and 428.49 kN (inner). When the flat length increases to 50 mm, the peak shifts to 0.8–1.0 s and rises to 943.88 kN and 986.86 kN.

This difference is attributed to the change in the phase relationship between the excitations of the inner and outer wheels. A larger phase difference occurs for the 30 mm outer flat, limiting early impact superposition. In contrast, the reduced phase difference for the 50 mm outer flat leads to stronger phase coupling, resulting in a significantly amplified impact response. To further explain this phenomenon, a theoretical derivation is conducted. Let v denote the train speed, R the wheel radius, L the flat length, k the track stiffness, c the damping coefficient, and f_n the dominant system modal frequency. The wheel–rail re-contact time can be expressed as follows:

$$t_c = \frac{L}{v} + \Delta t_s \tag{14}$$

The time $\frac{L}{v}$ required for the train to pass over a wheel flat, with Δt_s representing the lag correction of the flexible system, can be approximated as:

$$\Delta t_s = \frac{\zeta}{2\pi f_n} \tag{15}$$

$$\zeta = \frac{c}{2\sqrt{kM}} \tag{16}$$

Here, ζ denotes the equivalent damping ratio and M the wheel–rail coupled mass. Increasing flat length extends the contact passage time and excites more system modes, resulting in stronger damping participation and delayed impact. As shown in Figs. 8(c) and 5, the 50 mm outer-wheel flat produces the most pronounced response, consistent with the findings of Ren[3].

*Corresponding author

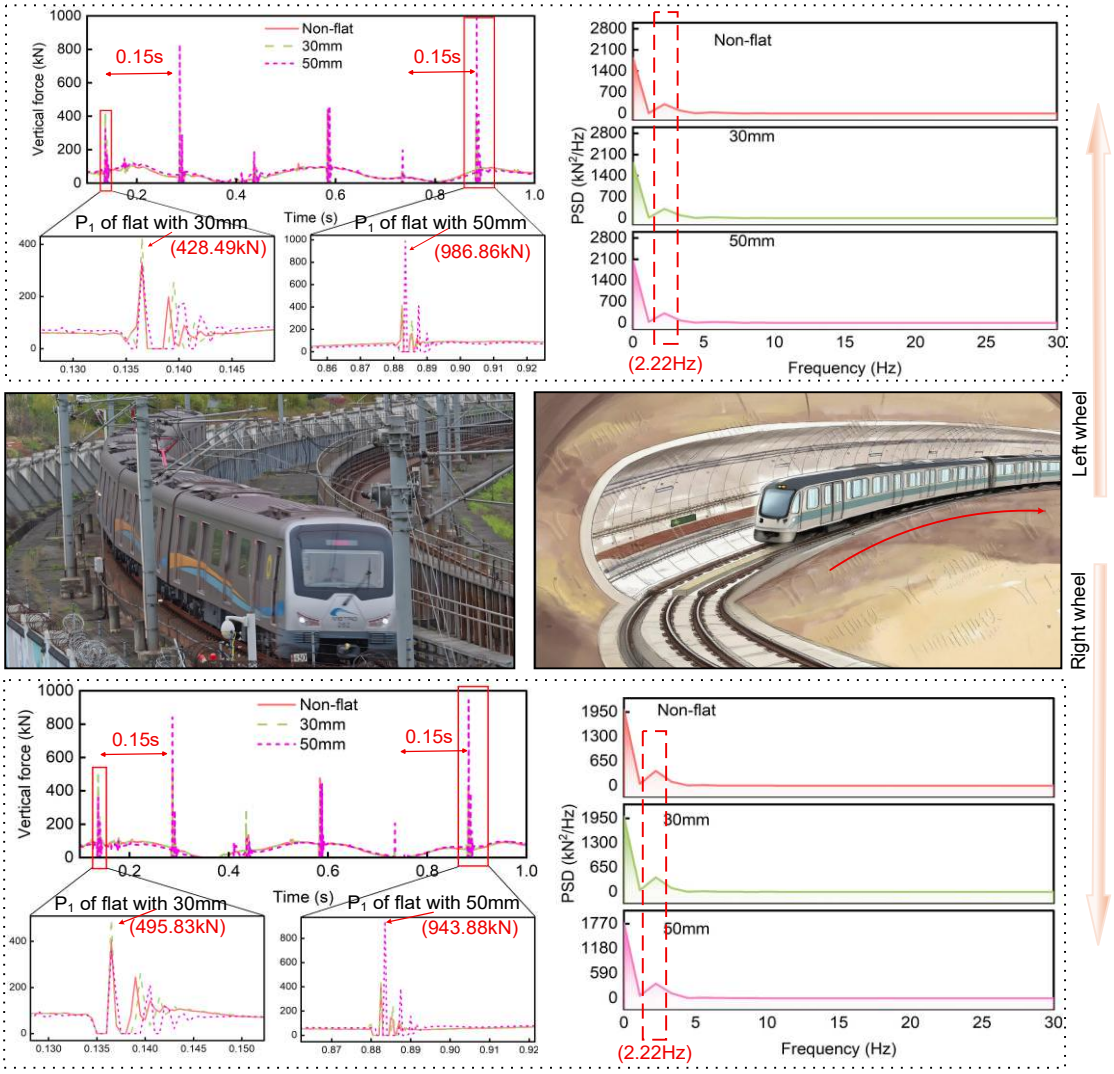


Fig. 9 Time-frequency domain analysis of vertical force in the left wheel without flat, 30mm and 60mm flat.

Frequency-domain analysis shows that the spectral energy of the wheel–rail system concentrates around 2.22 Hz for outer-wheel flat lengths of 0, 30, and 50 mm, close to the first bending modes of the rail and track slab (1.42 Hz). This indicates that the low-frequency response is governed by the global bending of the flexible track structure rather than the wheel-flat characteristic frequency. Wheel flats mainly redistribute spectral energy, producing a dominant peak at 2.22 Hz and a secondary peak at 5.56 Hz. The peak amplitudes increase with flat length, indicating an amplification effect.

3.2 Vibration Analysis under In-Phase Asymmetric Wheel-Flat Excitation

To investigate the influence of asymmetric wheel-flat excitation on track vibrations, representative pairs of continuous measurement points were selected to characterize the overall dynamic response of the track system. Multiple point pairs were arranged along the inner and outer rails and the corresponding sides of the track slab to form a spatially uniform observation network, allowing the longitudinal response characteristics to be captured more reliably. The measurement locations are illustrated in Figure. 10(a), with names consistent with the node numbering in the finite element model.

Five pairs of continuous measurement points were selected at rail fastener locations. According to the finite element model, the inner (outer) points were numbered 9 (9’), 10 (10’), 11 (11’), 12 (12’), and 13 (13’). The fastener spacing is 0.625 m, consistent with typical track structures and suitable for capturing the mid- to high-frequency responses of the rail–sleeper system.

*Corresponding author

In addition, three pairs of measurement points were arranged at the steel-spring locations, numbered 5 (5’), 6 (6’), and 7 (7’) for the inner (outer) sides. The spacing between adjacent spring pairs is 1.25 m (twice the fastener spacing), representing one structural span and allowing the low-frequency responses to be captured. Considering long-period excitation propagation, a 2.5 m spacing between spring pairs was also included to investigate coupled responses in the mid- to low-frequency range.

This measurement layout, combining fastener and spring observation points, enables a comprehensive evaluation of track vibration characteristics under asymmetric excitation from local to global scales and across a wide frequency range.

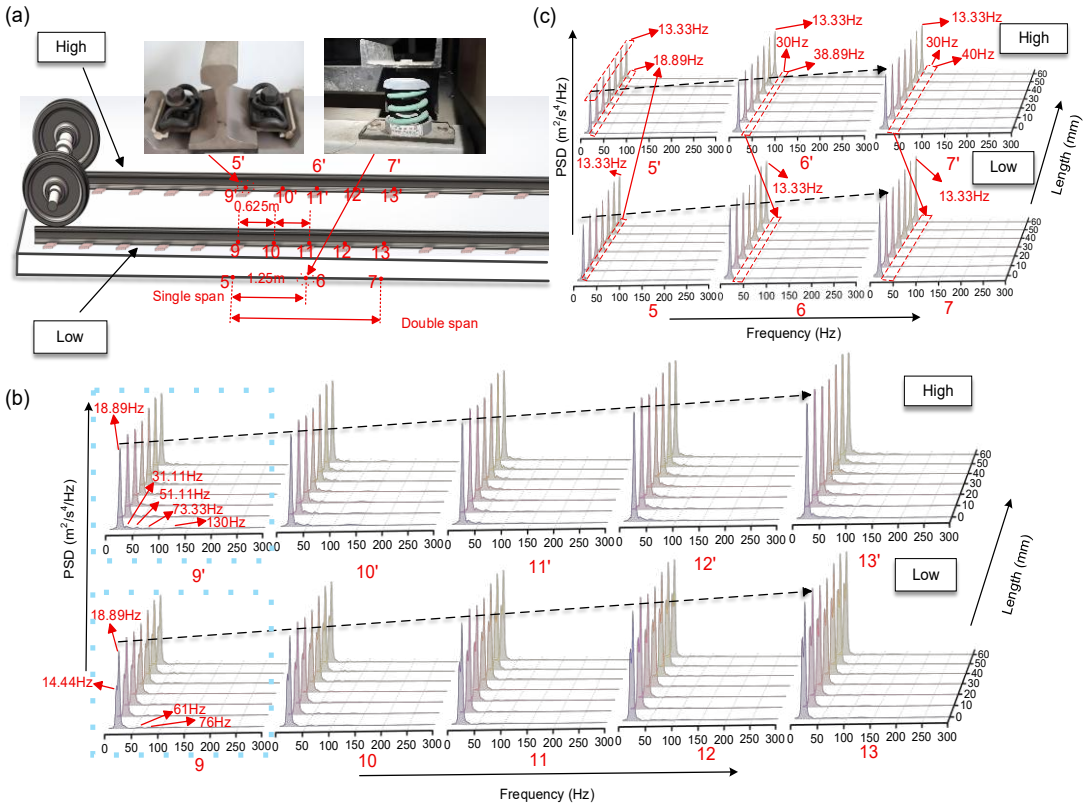


Fig. 10 Frequency domain analysis of vertical acceleration: (a) structure of the rail system. (b) frequency domain analysis of vertical acceleration with rail. (c) frequency domain analysis of vertical acceleration with floading slab.

Figure 10(b) presents the vertical acceleration power spectral density (PSD) at representative inner and outer rail measurement points within the 0–300 Hz range. In the control case without an outer-wheel flat (0 mm), the outer rail points exhibit consistent frequency responses, with a dominant peak at 18.89 Hz corresponding to the fifth vertical bending mode of the rail. Secondary peaks appear at 31.33 Hz, 51.11 Hz, 73.33 Hz, and 130 Hz, associated with the sixth, ninth, tenth, and twelfth modes, respectively.

Although the longitudinal spacing of measurement points increases, the peak frequencies remain unchanged, indicating spatial consistency of the modal characteristics. However, the PSD amplitudes gradually increase along the rail, suggesting energy accumulation during vibration propagation.

Under asymmetric wheel-flat excitation (outer-flat length 10–60 mm), the peak frequencies remain unchanged but the PSD amplitudes become unevenly distributed. Notably, when the outer-wheel flat length reaches 50 mm, several measurement points exhibit the highest PSD amplitudes, indicating stronger energy input due to enhanced coupling between the excitation and structural modal frequencies.

A similar trend is observed at the inner rail measurement points. Within the 0–300 Hz , the dominant peak remains at 18.89 Hz, consistent with the outer rail, indicating that the primary modal response of the

*Corresponding author

system is largely unaffected by lateral wheel–rail differences. Secondary peaks occur at 14.44 Hz, 61 Hz, and 76 Hz, corresponding to the fourth, ninth, and tenth vertical rail modes.

As with the outer rail, increasing longitudinal spacing does not change the peak frequencies but leads to higher PSD amplitudes, confirming energy amplification along the track direction. Notably, PSD amplitudes at inner rail points are significantly higher than those at the corresponding outer rail points, indicating stronger vibration energy accumulation on the inner rail under asymmetric wheel-flat excitation.

This behavior mainly results from asymmetric wheel–rail forces in curved track sections. The inner wheel experiences higher vertical contact forces due to centrifugal effects, producing stronger excitation of the inner rail. In addition, outer-wheel flat excitation can transfer energy to the inner rail through lateral coupling of the wheelset, potentially inducing additional responses or local resonance. Structural asymmetry in wheel–rail contact stiffness and boundary conditions further promotes energy accumulation at the inner rail.

Figure 10(c) shows the vertical acceleration PSD at representative floating-slab measurement points within 0–300 Hz. The dominant peak appears at 13.33 Hz, corresponding to the fourth bending mode of the floating slab. With increasing spacing between measurement points, secondary peaks shift to higher frequencies: 18.89 Hz at point pair 5, 30 Hz and 38.89 Hz at pair 6, and 30 Hz and 40 Hz at pair 7, corresponding to higher-order bending modes. This indicates that longer spans tend to excite higher-order structural modes. Meanwhile, PSD amplitudes increase with span, suggesting higher sensitivity of long-span structures to low-frequency excitation. Inner-side measurement points consistently exhibit higher PSD amplitudes than outer-side points, consistent with the energy distribution observed in the rails.

Notably, when the outer-wheel flat length reaches 50 mm, all floating-slab points show significantly elevated PSD amplitudes, indicating strong dynamic excitation of the slab system. Overall, under asymmetric wheel-flat excitation, peak frequencies are governed by structural modes, whereas wheel flats mainly modulate spectral energy amplitudes across the wheel–rail–track system.

4 Out-of-Phase Asymmetric Wheel-Flat Excitation on Track Dynamics

Wheel-flat defects occur at random circumferential positions on the wheel, and dual flats often exhibit a phase difference. This phase difference can significantly influence the superposition of excitation energy and the resulting dynamic response of the system. Therefore, investigating track dynamic behavior under different phase differences is essential for understanding defect coupling mechanisms and evaluating fatigue risk.

4.1 Vehicle–Track Dynamics under Phase-Shifted Asymmetric Wheel Flats

To examine the influence of phase difference on the dynamic response of the wheel–rail system under asymmetric dual wheel-flat excitation, nine phase differences between the inner and outer flats (5°–45°) were analyzed. The maximum vertical forces of both wheels were extracted for different outer-wheel flat lengths. Results show that, for most phase differences, the maximum vertical forces increase with flat length and peak at 50 mm. However, the peak amplitudes vary markedly with phase difference, with 25°, 30°, and 35° producing the most pronounced dynamic responses.

At an outer-flat length of 50 mm, increasing the phase difference from 5° to 25° raises the outer-wheel peak from 449.87 kN to 487.96 kN (+8.46%), while the inner-wheel peak decreases from 493.04 kN to 413.71 kN (−16.06%), indicating strong left–right asymmetry. At 30°, the outer-wheel peak further increases to 507.68 kN (+12.83% vs. 5°), whereas the inner-wheel peak reaches 434.13 kN (−11.93%), showing enhanced outer-wheel excitation and suppressed inner-wheel response.

When the phase difference increases to 35°, the outer-wheel peak drops to 445.67 kN (−12.20% vs. 30°), while the inner-wheel peak rises to 514.52 kN (+18.49%), indicating a reversal in peak trends and a reduced force difference between the wheels, suggesting partial cancellation of dual-wheel impacts. These results demonstrate that phase difference strongly affects the time-domain superposition of dual wheel-flat excitations, leading to significant variations in wheel–rail force amplitudes and left–right asymmetry.

As shown in Fig. 11(b) and (c), when the phase difference exceeds 25° and the wheel-flat length is below 30 mm, the maximum vertical forces of both wheels are significantly higher than those under the in-phase condition, indicating a superposition effect of dual excitations. In this case, the two wheel-flat impacts partially coincide in time, producing additive impact peaks. When the flat length reaches 40 mm, the

*Corresponding author

35° phase-difference condition yields the highest wheel–rail vertical force among all tested cases, suggesting near-resonant coupling between the excitation and a structural mode, which leads to local dynamic amplification.

However, as the flat length further increases to 40–50 mm, the contact force becomes lower than that under the in-phase condition. This reduction results from phase-offset excitations that partially cancel high-frequency components in both time and frequency domains, thereby weakening the vertical impact peaks.

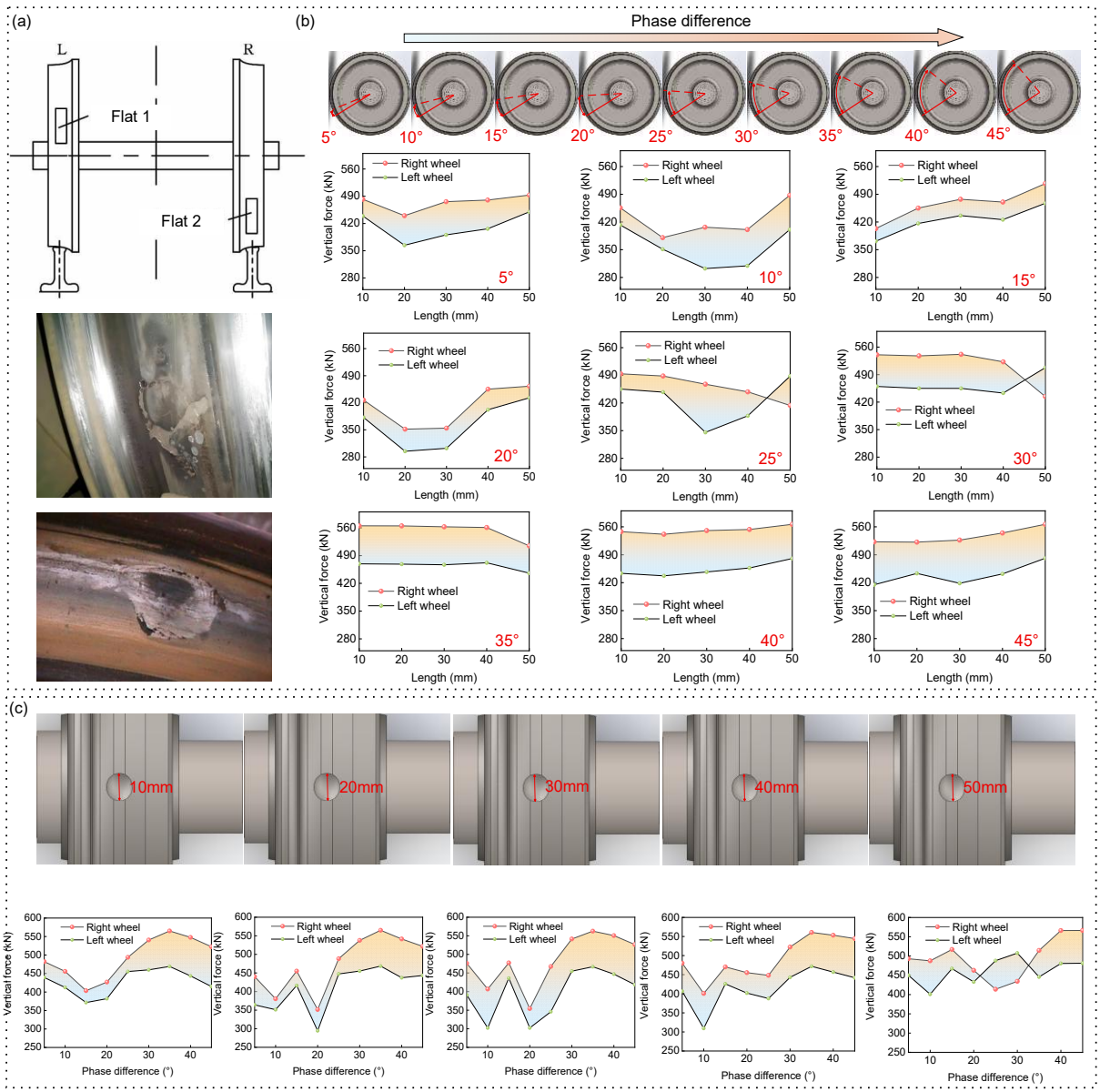


Fig. 11 Variation of maximum vertical wheel–rail forces of left and right wheels under different phase differences and outer wheel flat lengths: (a) schematic working condition. (b) comparison of maximum vertical wheel–rail forces of left and right wheels under different wheel flat length for the same phase differences. (c) comparison of maximum vertical wheel–rail forces of left and right wheels under different phase differences for the same outer wheel flat length.

As shown in Figure. 12(a) and (b), with increasing phase difference, the longer wheel flat (60 mm) tends to behave as a dominant single excitation in the time domain, generating an isolated impact pulse that does not coincide with the second flat. When the second flat (50 mm) partially overlaps in time, the superposition effect across several frequency bands becomes weaker than in the in-phase case, although some amplitude enhancement remains. Compared with the single 60 mm flat case, the vertical wheel–rail forces under

*Corresponding author

dual-flat excitation remain elevated across all phase differences. This indicates that even when phase offset reduces part of the superimposed energy, the second flat still injects additional vibration energy near the system's natural frequencies.

Therefore, the high-amplitude response under dual-flat excitation results not only from in-phase superposition but also from sustained energy input from multiple excitation sources.

Table 3 Maximum vertical wheel–rail forces of left and right wheels under combinations of phase difference and outer wheel flat length.(High: wheel that interact with the high rail. Low: wheel that interact with the low rail.)

Phase difference (°)	Maximum vertical force of the wheels (kN)									
	10mm		20mm		30mm		40mm		50mm	
	High	Low	High	Low	High	Low	High	Low	High	Low
5°	439.15	482.09	364.06	440.08	390.73	476.08	406.33	480.27	**449.87**	**493.04**
10°	412.34	455.73	351.25	380.5	302.37	406.86	309.28	400.83	400.68	487.42
15°	371.41	403.46	416.25	455.1	436.17	477.36	425.81	470.4	467.16	516.97
20°	381.88	426.85	294.52	351.69	302.32	354.41	401.89	455.22	432.81	462.88
25°	455.23	493.86	447.39	488.28	345.72	467.51	387.61	448.18	**487.96**	**413.71**
30°	459.91	540.52	455.01	537.67	454.91	541.56	443.07	522.49	**507.68**	**434.13**
35°	469.15	565.07	468.41	564.83	466.81	562.54	471.89	560.78	**445.67**	**514.52**
40°	443.38	547.79	437.23	541.4	446.86	550.58	456.85	553.31	480.56	566.19
45°	414.78	522.38	443.22	521.65	418.46	526.7	441.95	544.54	481.24	566.28

PSD analysis shows that under dual-flat excitation the outer wheel exhibits higher amplitudes than the inner wheel, indicating stronger vertical dynamic loading. Pronounced peaks at 36 Hz and 60 Hz correspond to the 7th and 9th vertical modes of the rail–floating slab system, revealing resonance coupling between excitation energy and structural modes. This coupling is more evident on the outer-wheel side, amplifying vertical force peaks and explaining the high-amplitude response under dual-flat excitation. These results agree with the time-domain observations, confirming the stronger vertical dynamic response of the outer wheel.

*Corresponding author

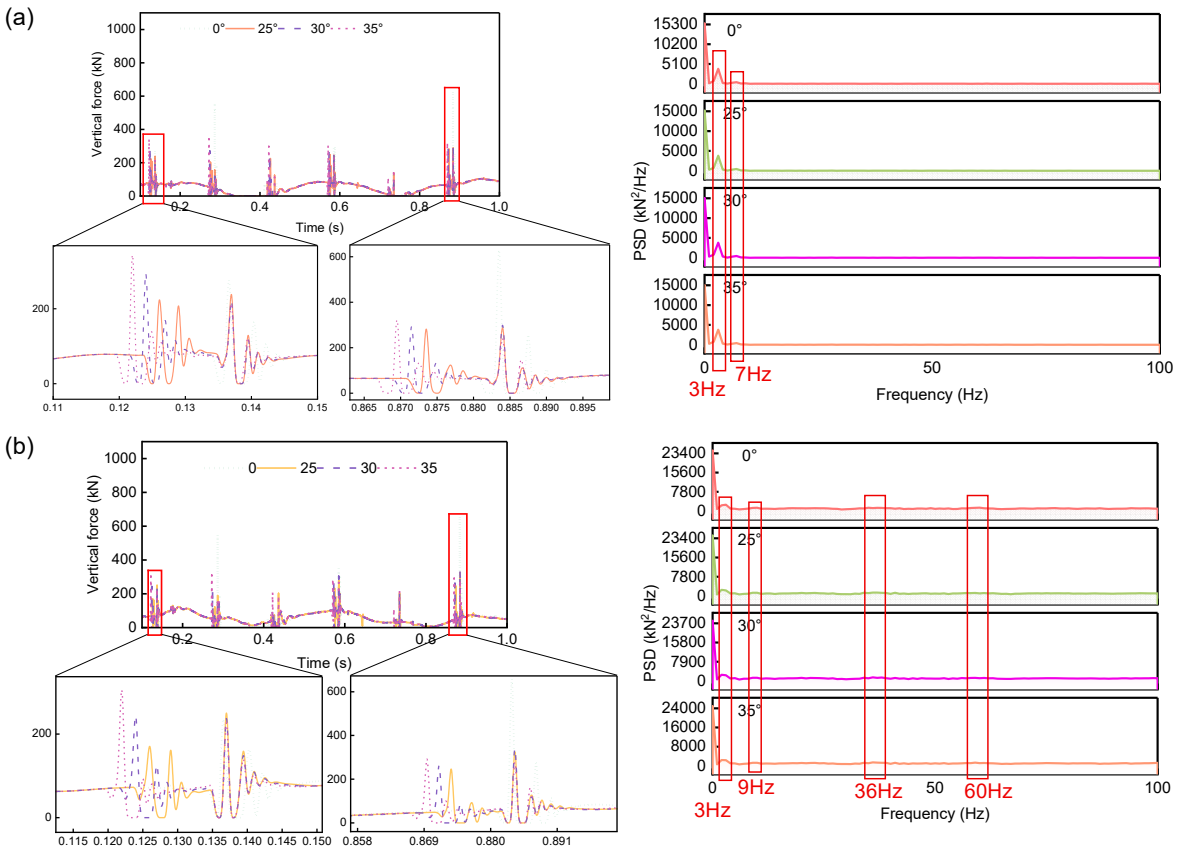


Fig. 12 Time-frequency domain analysis of the left and right wheels with phase differences of 0°, 25°, 30°, and 35°: (a) time-frequency domain analysis of right wheel. (b) time-frequency domain analysis of the left wheel.

4.2 Vibration Analysis of Track System under Non-Synchronous Asymmetric Dual-Flat Excitation

Under asymmetric dual-flat excitation, with outer-wheel flat lengths ranging from 10 to 50 mm and phase differences of 5°–45°, the vertical acceleration PSD at multiple inner and outer rail and track-slab measurement points was obtained from dynamic simulations. The results show that, within the 10–50 mm flat-length range, the dominant PSD frequencies remain nearly unchanged, and the overall spectral shape and peak positions vary little. Because the 50 mm outer-flat condition produces the strongest response, it is selected for detailed analysis. As shown in Fig. 13(a) and (b), the PSD of vertical acceleration for the rail and track slab is presented, with the numbers in parentheses indicating different phase differences.

The results indicate that phase difference mainly affects PSD amplitudes rather than peak frequencies. The outer rail exhibits a dominant peak at 18.89 Hz, while the inner rail shows peaks at 18.89 Hz and 14.44 Hz. For the track slab, both inner and outer points display peaks around 13.33 Hz. These frequencies correspond to the fourth-order vertical vibration modes of the rail–track slab system, indicating that the inherent structural modes are effectively excited under asymmetric dual-flat excitation.

The stability of the dominant frequencies is governed by the system's natural frequencies. The inherent frequencies of the rail–track slab system are determined by structural stiffness, mass, and boundary conditions. Although variations in flat length modify the spatiotemporal characteristics of the excitation, they do not change these intrinsic frequencies. As local excitation sources, wheel flats inject energy that is amplified near the structural modal frequencies, producing stable PSD peaks. Thus, flat length mainly affects excitation energy distribution and peak amplitudes, with little influence on peak positions. The dual peaks observed on the inner rail at 14.44 Hz and 18.89 Hz are attributed to differences in inner–outer rail constraints, structural coupling, and phase interference between multiple defects. Combined with the previous phase-difference analysis, it is evident that phase primarily modulates response amplitudes and spatial

*Corresponding author

synchrony across measurement points without altering the system's natural frequencies, thereby preserving PSD peak locations.

Overall, within the investigated range, flat length does not change the frequency response characteristics of the structure, whereas phase difference mainly affects amplitude distribution. From an engineering perspective, the 13.33–18.9 Hz band is recommended as a key feature range for online monitoring and defect identification, where amplitude, phase, and time–frequency energy characteristics can be jointly used for quantitative detection and fatigue assessment.

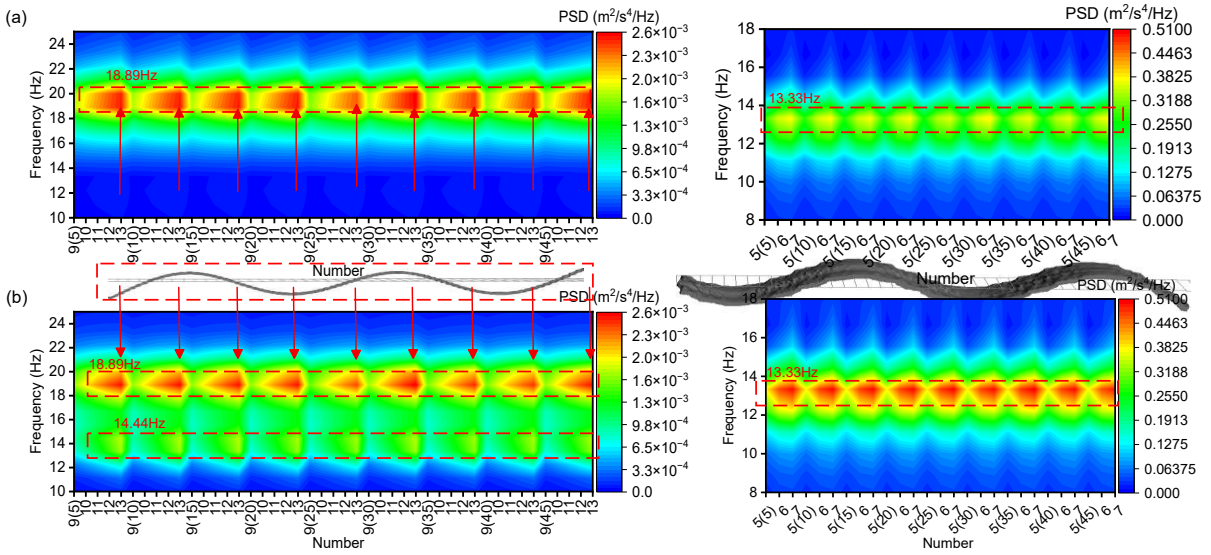


Fig. 13 Frequency domain analysis of vertical acceleration of the rail and floading slab: (a) vertical vibration acceleration of rail with 50mm flat on outer wheel: frequency domain analysis underdifferent phase difference. (b) vertical vibration acceleration of floading slab with 50mm flat on outer wheel: frequency domain analysis underdifferent phase difference.

5 Conclusion

This study investigated the dynamic responses of rails and track slabs under varying wheel-flat lengths and phase differences. The results clarify how wheel-flat excitation affects wheel–rail vertical forces and vibration characteristics of the track system, providing insights into vibration mechanisms and defect identification. The main findings are summarized as follows:

(1) The minimum response occurs at 30 mm due to partial cancellation between the excitations induced by the two wheel flats, whereas the maximum increase appears at 50 mm because of strong phase coupling. Frequency-domain results indicate that the dominant vibration energy is concentrated around 2.22 Hz, which is close to the first bending mode of the rail–track slab system (1.42 Hz). This suggests that the low-frequency response is primarily controlled by the structural modal characteristics, while the flat length mainly influences the response amplitude.

(2) Under asymmetric wheel-flat excitation with outer-wheel flat lengths ranging from 10 to 60 mm, the peak frequencies remain nearly unchanged, whereas the spectral amplitudes vary significantly, with the 50 mm condition producing the strongest response because of pronounced modal coupling. The inner rail generally shows higher PSD amplitudes than the outer rail, with secondary peaks at 14.44 Hz, 61 Hz, and 76 Hz, indicating stronger vibration energy concentration on the inner rail. For the floating slab, the dominant response occurs at 13.33 Hz, associated with its fourth bending mode, while longer flat lengths further excite higher-order modes; overall, the system peak frequencies are determined mainly by structural modal characteristics, whereas wheel flats primarily affect vibration amplitude and energy distribution.

(3) Under asymmetric dual-flat excitation with an outer-flat length of 10–60 mm and a phase difference of 5°–45°, the maximum wheel–rail force occurs at an outer-flat length of 50 mm and a phase difference of about 30°, where the outer-wheel peak reaches 507.68 kN and the inner-wheel peak decreases to 434.13 kN, indicating a pronounced left–right asymmetric superposition effect. When the phase difference

*Corresponding author

increases to 35°, the peak forces of the two wheels are reversed, suggesting partial cancellation of the dual-flat impact. Frequency-domain results show that the outer wheel exhibits stronger vibration amplitudes than the inner wheel, with dominant peaks at 36 Hz and 60 Hz corresponding to the seventh and ninth vertical modes of the rail–floating slab system. These results indicate that the multi-source excitation induced by dual flats can couple with structural modal resonance, thereby amplifying the vertical force response of the outer wheel.

(4) Under outer-wheel flat lengths of 10–50 mm and phase differences of 5°–45°, the dominant vertical acceleration PSD frequencies at the rail and track slab measurement points remain essentially unchanged. The outer rail is dominated by a peak at 18.89 Hz, the inner rail shows two main peaks at 18.89 Hz and 14.44 Hz, and the track slab peaks around 13.33 Hz, indicating that the system response is primarily governed by the structural natural frequencies. In contrast, the wheel flat length and phase difference mainly affect the response amplitude, energy distribution, and spatial synchrony, with the 50 mm flat producing the most significant dynamic effect. Therefore, the 13.33–18.89 Hz frequency band can be considered a key indicator for online monitoring and defect identification of track systems.

Author contributions Zijie Xu conducted the simulations and experiments and drafted the manuscript. Xinlei He and Sisi Li collected and processed the data. Xiang Li, Zunsong Ren, and Hui Fan supervised the experimental and simulation work and provided guidance on the writing of the manuscript. All authors contributed to the preparation of the paper and approved the final manuscript.

Funding information The authors acknowledge the support of the National Natural Science Foundation of China(U2368215), Jiangsu Provincial Natural Science Foundation Project(BK20231352).

Data availability The datasets generated during and/or analyzed during the current study are available from the corresponding author on reasonable request.

Declarations

Competing interests The authors declare no competing interests.

Reference

1. Zhai, W.M., Wang, Q.C., Lu, Z.W., Wu, X.S.: Dynamic effects of vehicles on tracks in the case of raising train speeds. Proc. Inst. Mech. Eng. Part F J. Rail Rapid Transit 215(2), 125-135 (2001).
2. Zhu, J.J., Ahmed, A.K.W., Rakheja, S., Hu, Y.S.: Impact load due to railway wheels with multiple flats predicted using an adaptive contact model. Proc. Inst. Mech. Eng. Part F J. Rail Rapid Transit 223(4), 391-403 (2009).
3. Ren, Z.S.: An investigation on wheel/rail impact dynamics with a three-dimensional flat model. Veh. Syst. Dyn. 57(3), 369-388 (2019).
4. Li, Y.F., Zuo, M.J., Lin, J.H., Liu, J.X.: Fault detection method for railway wheel flat using an adaptive multiscale morphological filter. Mech. Syst. Signal Process. 84, 642-658 (2017).
5. Zhou, C.Y., Gao, L., Xiao, H., Hou, B.: Railway wheel flat recognition and precise positioning method based on multisensor arrays. Appl. Sci. 10(4), 1297 (2020).
6. Magalhães, J., Jorge, T., Silva, R., Guedes, A., Ribeiro, D., Meixedo, A., Mosleh, A., Vale, C., Montenegro, P., Cury, A.: A strategy for out-of-roundness damage wheels identification in railway vehicles based on sparse autoencoders. Railw. Eng. Sci. 32(4), 421-443 (2024).
7. Fu, W.J., He, Q.X., Feng, Q.B., Li, J.K., Zheng, F.J., Zhang, B.: Recent advances in wayside railway wheel flat detection techniques: A review. Sensors 23(8), 3916 (2023).
8. Uzzal, R.U.A., Ahmed, W., Bhat, R.B.: A three-dimensional modeling study of wheel/rail impacts created by multiple wheel flats, and the development of a smart wheelset. Proc. Inst. Mech. Eng. Part F J. Rail Rapid Transit (2014), 0954409714545558.
9. Nielsen, J.C.O., Johansson, A.: Out-of-round railway wheels-a literature survey. Proc. Inst. Mech. Eng. Part F J. Rail Rapid Transit 214(2), 79-91 (2000).
10. Jin, X.S., Wu, L., Fang, J.Y., Zhong, S.Q., Ling, L.: An investigation into the mechanism of the polygonal wear of metro train wheels and its effect on the dynamic behaviour of a wheel/rail system. Veh. Syst. Dyn. 50(12), 1817-1834 (2012).

*Corresponding author

11. Ye, Z.R., Chen, Z.G., Zhou, Z.W., Xu, Y.H.: Effect of wheel polygonization on the dynamic response of the electromechanical coupling system in a permanent magnet direct-drive locomotive. Proc. Inst. Mech. Eng. Part F J. Rail Rapid Transit 239(6), 507-517 (2025).
12. Xu, Z.J., Li, X., He, X.L., Wang, Z., Ma, J., Fan, H.: Impact of wheel polygonization on vehicle vibration and wheel-rail interaction forces. Noise Vib. Worldw. (2025), 09574565251359155.
13. Ye, Y.G., Qu, S., Wei, L., Li, D.D., Huang, C.H., Wang, J.B., Tao, Z.C., Gan, F., Gao, H., Zhu, B., Wu, P.B., Zeng, J., Dai, H.Y.: Localized rail third-order bending mode causes high-order polygonization of high-speed train wheels. Mech. Syst. Signal Process. 223, 111816 (2025).
14. Wang, J.T., Ding, X., Liu, Z.D., Teng, W.X., Liu, T., Li, Y.S.: An experimental study on abnormal vibration of metro trains caused by out-of-round wheels. Proc. Inst. Mech. Eng. Part F J. Rail Rapid Transit 237(2), 224-231 (2023).
15. Hu, J.Y., Zheng, Z.G., Xu, J.M., Qian, Y., Lai, J., Wang, P.: Characteristics of rail corrugation in metro turnouts and their effects on the dynamic response of the vehicle-turnout system. Eng. Fail. Anal. 169, 109215 (2025).
16. Cui, D.B., Li, L., Wang, H.Y., Wen, Z.F., Xiong, J.Y.: High-speed EMU wheel re-profiling threshold for complex wear forms from dynamics viewpoint. Wear 338, 307-315 (2015).
17. Luo, W., Wang, B.J., Wang, W.J., Li, Q., Liu, X.: Track structure influence analysis on metro bogie frame dynamic stress with a rigid-flexible coupled model. Eng. Fail. Anal. 171, 109357 (2025).
18. Wang, Y., Xiao, H., Nadakatti, M.M., Zhang, Z.H., Chi, Y.H., Lin, X.B.: A metro rail corrugation detection framework based on car body vibration signals and unsupervised learning. Eng. Appl. Artif. Intell. 153, 110976 (2025).
19. Wang, Z.Q., Lei, Z.Y., Luo, Y.Y.: Cause analysis of rail corrugation in metro lines based on system vibration characteristics. Chin. J. Mech. Eng. 37(1), 147 (2024).
20. Wang, Z.Q., Zhu, J.Y.: Wheel-rail stick-slip characteristics under coupling damages of rail corrugation and wheel flat in metro. KSCE J. Civ. Eng. 28(4), 1321-1335 (2024).
21. Wu, B.W., Tang, T.C., Pan, J.B., Zhang, R.Y., Xu, R., Ye, D.D., Chen, Y.J.: Effect of the wheelset structure on short-pitch corrugation on tight curved track of metro. Wear 523, 204831 (2023).
22. Zhu, G.N., Du, X.G., Liu, W., Cao, Q.J., Lu, K., Guo, Y.S., Yang, T., Chen, Y.S., Wei, C.Z., Pu, J.L.: A novel method to solve the existed paradox of low-frequency vibration isolation and displacement attenuation in a nonlinear floating-slab on the wheel-rail loads. Mech. Syst. Signal Process. 208, 110985 (2024).
23. Luo, Y.F., Tao, G.Q., Tan, C.W., Wen, Z.F., Wang, W.J., Zhang, W.J.: Numerical study on local wheel temperature induced by wheel flat during tread braking. Int. J. Therm. Sci. 218, 110176 (2025).
24. Li, X.: Study on vibration and rail corrugation of metro vibration-reduction track structure. Beijing Jiaotong University, Beijing (2019) (in Chinese).
25. Zhou, Z.W., Chen, Z.G., Spiryagin, M., Arango, E.B., Wolfs, P., Cole, C., Zhai, W.M.: Dynamic response feature of electromechanical coupled drive subsystem in a locomotive excited by wheel flat. Eng. Fail. Anal. 122, 105248 (2021).
26. Xu, J.M., Ma, Q.T., Zhao, S.Q., Chen, J.Y., Qian, Y., Chen, R., Wang, P.: Effect of wheel flat on dynamic wheel-rail impact in railway turnouts. Veh. Syst. Dyn. 60(6), 1829-1848 (2022).
27. Wu, X.W., Rakheja, S., Ahmed, A.K.W., Chi, M.R.: Influence of a flexible wheelset on the dynamic responses of a high-speed railway car due to a wheel flat. Proc. Inst. Mech. Eng. Part F J. Rail Rapid Transit 232(4), 1033-1048 (2018).
28. Dong, Z.Y., Wang, W.J., Zhang, K., Wang, Y.: Effects of wheel flats on vibration and stress response of the wheel-rail system in high-speed trains. Int. J. Struct. Stab. Dyn. 26(05), 2650018 (2026).

*Corresponding author